EFFECTS OF FIBER ORIENTATION AND CONTENT ON THE STATIC AND FATIGUE BEHAVIOR OF SFRC BY USING CT-SCAN TECHNOLOGY

Miguel A. Vicente[a,*], Gonzalo Ruiz[b], Dorys C. González[a]. Jesús Mínguez[a], Manuel Tarifa[c], Xiaoxin Zhang[b]

[a] E. Politécnica Superior, Universidad de Burgos, Campus Milanera (Edif. D), c/ Villadiego s/n, 09001 Burgos, Spain

[b] ETSI de Ingenieros de Caminos, C. y P., Universidad de Castilla-La Mancha, Avda. Camilo José Cela s/n, 13071 Ciudad Real, Spain

[c] ETSI Aeronáutica y del Espacio, Universidad Politécnica de Madrid, Plaza del Cardenal Cisneros, 3, 28040 Madrid, Spain.

* Corresponding Author: mvicente@ubu.es

Keywords: fiber-reinforced concrete; CT-Scan technology; crack patterns; fatigue.

ABSTRACT

The effects of the fiber orientation and content on the behavior of steel fiber-reinforced concrete (SFRC) under static and cyclic compressive loads are studied using the computed tomography (CT) technique, and the resistance mechanisms of the fibers are carefully observed. The results suggest that the intrinsic scatter in the fatigue life could be partially explained by the essential scatter in the fiber orientation and content. On the contrary, no relationship is observed between the intrinsic scatter in compressive strength and fiber orientation and content, which suggests that the compressive strength of the specimens is mainly due to their concrete matrix.

1. INTRODUCTION

It is well known that many structural parameters of concrete elements, such as compressive and tensile strength, Young's Modulus and fatigue life, among many others, show an essential scatter. Observation of concrete fatigue life commonly yields experimental results that can vary by two orders of magnitude when "identical" concrete specimens subjected to "identical" cyclic loads, are compared. This scatter effect is observed not only in plain concrete, but also in fiber-reinforced concrete (FRC). Moreover, in the case of FRC specimens, the intrinsic scatter is even more intense.

Scatter is a problematic design issue because it leads to excessively conservative design specifications, so that structural safety during service life is beyond any doubt. However, over-conservative specifications negatively affect the design and the optimization of structural elements, especially in the case of precast and consequently, productive solutions. A good example of this issue can be observed in concrete structures where fatigue failure is the most restrictive criterion, and as a consequence, the structures are designed according to this failure, as occurs in the case of precast concrete specimens for wind turbine towers [1, 2]. Strict safety factors are specified in the current international standards [3, 4], resulting in very significant underestimations of the mechanical capacity of the concrete.

The main cause of the intrinsic scatter of concrete can be found in the randomness of its internal microstructure [5-14]. Concrete is a strong heterogeneous material, where both coarse and fine aggregates, among other components, show random shapes that are also randomly positioned within the matrix. Moreover, concrete and its setting and hardening processes result in the presence of pores, voids and microcracks, which are likewise random in nature (shape, size, position, orientation, etc.). In the case of fiber-reinforced concrete, we may also refer to the intrinsic scatter of its fiber orientation and fiber position.

The intrinsic scatter of concrete is, to a lesser extent, due to the testing procedure. Regarding this topic, it is worth noting the research performed by Tarifa and co-workers [15] that emphasized how uncertainty in the loading position had a strong impact on the fatigue life of the concrete specimens.

Computed Tomography (CT) Scan technology is a very useful technique for studying the internal microstructure of matter. Regarding fiber-reinforced concrete, it forms the basis for understanding the interaction between the internal microstructure of concrete and its macroscopic behavior. CT is a non-destructive technique used to visualize the internal microstructure of materials based on the properties of X-rays. A CT-Scan device consists of an intensity-controlled X-ray source and a detector, which measures the loss of X-ray intensity. During the scanning process, X-rays are emitted in all directions, and the rays pass through every point of the sample from different directions. The detector measures and records the final X-ray intensity of all emissions.

In addition to its traditional use in medicine, this technology is currently widely used in concrete research, especially in fiber-reinforced concrete [16-23]. The enormous advantage of CT-Scan technology, in the case of FRC, is that it may obtain the exact position and orientation of each individual fiber, which is otherwise impossible with other techniques. Moreover, the combined use of CT-Scan technology with a macroscopic test is currently providing interesting results, since it is possible to correlate the internal microstructure with the macroscopic response. A detailed explanation of CT-Scan technology and its use in several engineering fields can be obtained in [24, 25].

The aim of this research is to analyze how the intrinsic scatter of fiber orientation and content influences compressive strength and fatigue life in fiber-reinforced concrete specimens tested under static and cyclic tests. Once the static and cyclic compressive loading was performed, all the specimens were scanned, in order to obtain their fiber orientation and content. Subsequently, the feasible correlations between fiber orientation and mechanical behavior (compressive strength and fatigue life) were discussed. Finally, a clear correlation between the orientation of the fiber with regards to the vertical axis, i.e., the loading axis and the fatigue life was observed.

In addition, the internal failure mechanisms were studied, by reusing the information provided by the CT-Scan, in order to better understand the resistance mechanisms of the fibers and their influence on the macroscopic response of the concrete specimen.

The structure of this paper is as follows: The experimental program is presented in Section 2; the experimental results are described and discussed in Section 3; the resistance mechanisms are shown in Section 4; and finally, the conclusions are drawn in Section 5.

2. EXPERIMENTAL PROGRAM

In this section, the materials, the testing procedure and scanning procedures will all be described.

2.1 Materials

The entire test campaign included 48 cubic specimens with an edge length of 40 mm, and which to two series: labeled A-Series and B-Series, respectively. Table 1 shows the mix proportions of each series.

Table 1: Mix proportions

Material	A-Series	B-Series
Type of cement	CEM I 52.5 SR	CEM I 42.5 R-SR
Cement (kg/m^3)	414.82	543.31
Fly ash (kg/m^3)		65.20
Siliceous filler (kg/m^3)	135.00	190.16
Sand I (0-0.8 mm) (kg/m^3)		657.40
Sand II (0-2 mm) (kg/m^3)	934.00	690.00
Gravel (kg/m^3)	717.00	
Water (kg/m^3)	183.89	206.46
Superplatizicer (kg/m^3)	4.98	11.41
Steel fiber (kg/m^3)	15.00	40.00
Steel fiber volume ratio	0.2%	0.5%

Portland Cement CEM I 42.5N R-SR and CEM I 52.5 SR [26], with coarse and fine aggregates of crushed limestone (maximum size 8 mm) were used. Straight smooth steel fibers of 13 mm in length and 0.2 mm in diameter were added to the concrete (commercial name: DRAMIX OL13/02, N.V. Bekaert S.A., Kortrijk, Belgium), together with Glenium 52 superplasticizer (BASF, Ludwigshafen, Germany). The concrete quality according to Eurocode 2 [27] was C45/55 for the A-Series and C90/105 for B-Series.

Regarding the mixing procedure for fabrication, the order of the addition of the components was from larger to smaller dry aggregates, including the filler in the last place, then cement, water and superplasticizer, respectively. At the end of the mixing process, when the concrete was almost ready, the fibers were added through a sieve to prevent the formation of fiber balls.

Slump flow tests for fresh concretes were performed for both series, and the results show that they exhibit similar behavior, that is the diameter of the spread was 670 mm for the A-Series and 700 mm for the B-Series. It should be borne in mind that the B-Series has more fiber content and smaller maximum aggregate size. Moreover, there is not a direct relationship between the fiber angles and the fresh test results.

Two prisms (one per series and mixture), with dimensions of 100×100×420 mm per mixture were fabricated. The specimens were cured for 180 days in a climatic chamber at a relative humidity of 97% ± 0.5% and an ambient temperature

of 20ºC ± 0.5ºC. They were then removed from the chamber and maintained under laboratory conditions until tested. All the specimens were at least 300 days-old at the start of the test campaign, so any possible strength increase during the fatigue test period was minimized.

A total of 32 cubic specimens with an edge length of 40 mm were cut from each prism (Figure 1). The procedure was as follows: First, the prisms were sawn into eight slices; then, from each slice four cubes were cut. The faces of each cube were grounded until they had an edge-length of approximately 40 mm, with a tolerance of ±0.2 mm. The borders of the prims were discarded, in order to avoid the "boundary effect" (especially in the case of fiber orientation) in the results. In this study, only 24 cubes were randomly selected from among the 32 cubes of each prism.

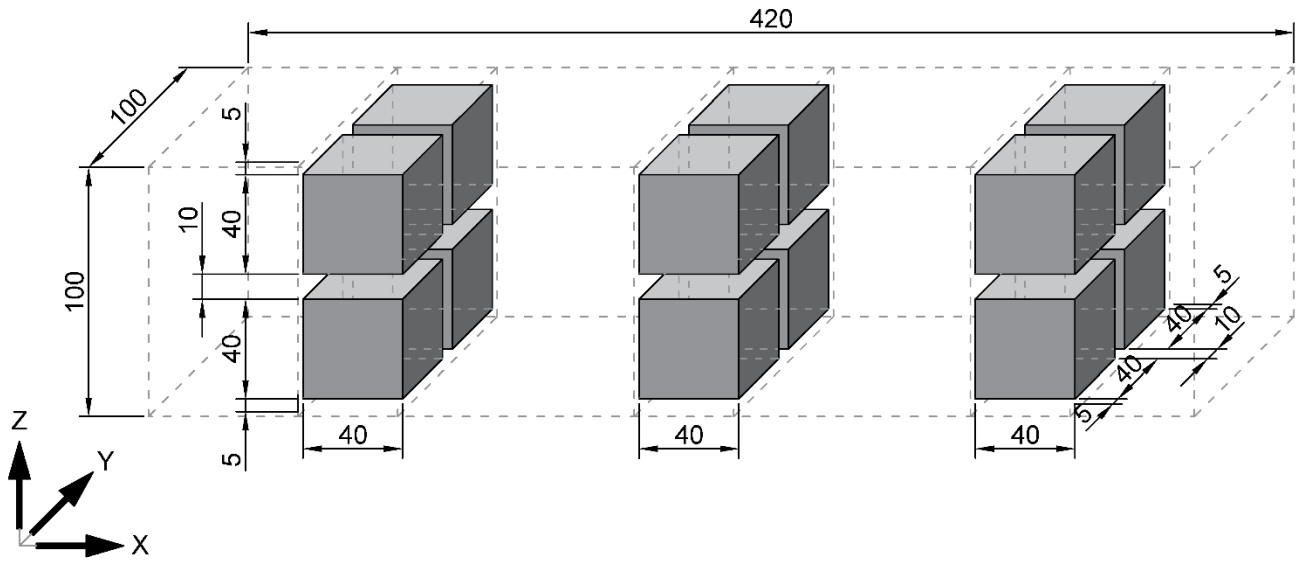

Figure 1: Specimens.

2.2 Static and cyclic testing

Twenty-four specimens of each series were tested. Eight from each series were tested under static compressive load until failure, and sixteen tests for each series were conducted under cyclic compressive load until failure. The average compressive strength of the mixture just prior to the fatigue tests was 53.6 MPa for the A-Series with a standard deviation of 1.8 MPa, and 127.7 MPa for the B-Series with a standard deviation of 5.3 MPa.

In the case of the A-Series, the cyclic load applied to each specimen ranged from 86% to 35% of the average compressive strength (obtained from the previous static tests). In the case of the B-Series, the cyclic load ranged from 88% to 24% of its average compressive strength. The expected theoretical fatigue life, "N", according to Model Code 2010 [3],

of 20ºC ± 0.5ºC. They were then removed from the chamber and maintained under laboratory conditions until tested. All the specimens were at least 300 days-old at the start of the test campaign, so any possible strength increase during the fatigue test period was minimized.

A total of 32 cubic specimens with an edge length of 40 mm were cut from each prism (Figure 1). The procedure was as follows: First, the prisms were sawn into eight slices; then, from each slice four cubes were cut. The faces of each cube were grounded until they had an edge-length of approximately 40 mm, with a tolerance of ±0.2 mm. The borders of the prims were discarded, in order to avoid the "boundary effect" (especially in the case of fiber orientation) in the results. In this study, only 24 cubes were randomly selected from among the 32 cubes of each prism.

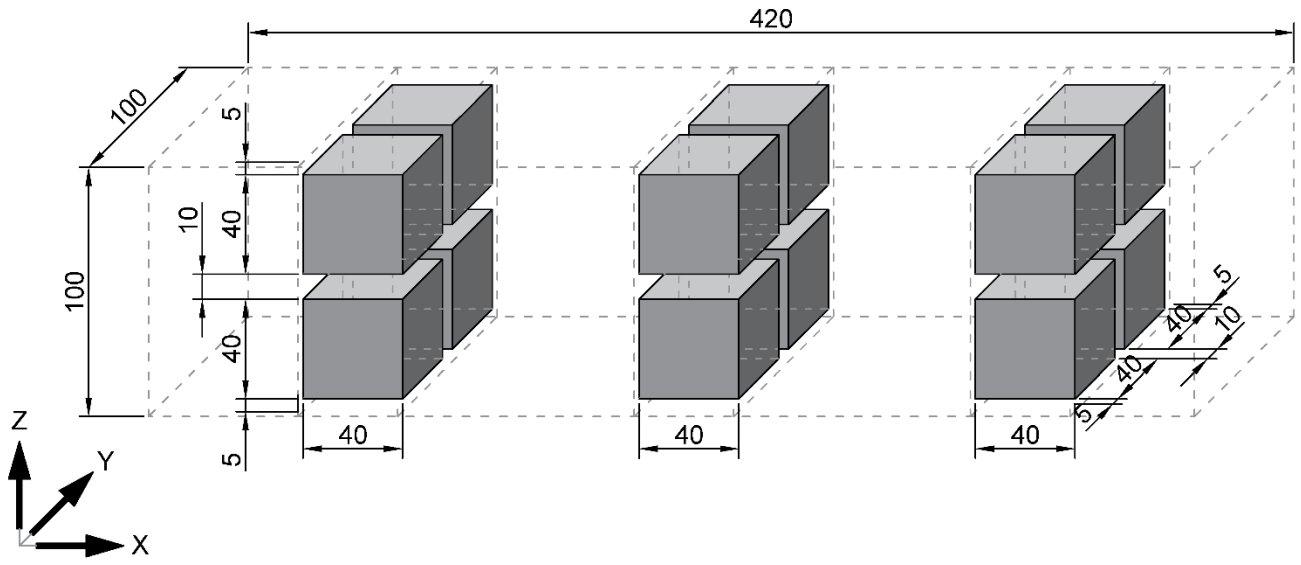

Figure 1: Specimens.

2.2 Static and cyclic testing

Twenty-four specimens of each series were tested. Eight from each series were tested under static compressive load until failure, and sixteen tests for each series were conducted under cyclic compressive load until failure. The average compressive strength of the mixture just prior to the fatigue tests was 53.6 MPa for the A-Series with a standard deviation of 1.8 MPa, and 127.7 MPa for the B-Series with a standard deviation of 5.3 MPa.

In the case of the A-Series, the cyclic load applied to each specimen ranged from 86% to 35% of the average compressive strength (obtained from the previous static tests). In the case of the B-Series, the cyclic load ranged from 88% to 24% of its average compressive strength. The expected theoretical fatigue life, "N", according to Model Code 2010 [3],

was approximately three thousand cycles for the A-Series and four houndred cycles for the B-Series. It is worth noting that any stress level would be valid for the study of the relationship between the fiber distribution and fatigue life.

All tests were performed with a servo-hydraulic INSTRON machine (INSTRON, Norwood, MA, USA), capable of applying 250 kN of load and equipped with a spherical seat, The INSTRON T1086-53 model with a radius of 95 mm, ensured that the loading axis coincided with the axis of the actuator and the load cell (see Figure 2).

Figure 2: Test.

All the specimens were wrapped in a PVC cling film prior to the mechanical tests, in order to prevent the specimen fragmentation once the failure point had been reached. Moreover, an end-of-test condition was programmed in the test machine. In the case of the static tests, the end-of-test criterion ensured that the test ended when the vertical load dropped by more than 20% of the maximum load. In the case of the cyclic tests, the end-of-test criterion ensured that the test ended when the required vertical displacement of the piston rod reached a load that was 20% greater than the one required in the previous cycle. In both cases, these end-of-test conditions, in combination with the PVC cling film, meant that none of the specimens underwent an explosive collapse.

2.3 CT-Scan test

After performing the mechanical tests, all the specimens were scanned in order to visualize the internal microstructure of the concrete. CT-Scan technology permitted a close-up examination of fiber locations and orientations in each specimen after the static and fatigue tests.

In this research, the cubic specimens were CT-scanned by a GE Phoenix v|tome|x device (General Electric, Boston, MA, USA) equipped with a 300 kV/500W tube. The intensity-controlled X-ray source emits a cone ray that is received by an array of detectors, which measures the loss of X-ray intensity, depending on the density of the matter along its path. More detailed information about CT-Scan technology can be found in [24] and [25].

By using a post-processing software package, a total of 1,334 2D slices with pixel sizes of 2048×2048 (Figure 3) were obtained throughout the height of the specimen from the CT-scan data. In this case, the horizontal resolution was approximately 30x30 μm^2 and the vertical distance between the slices was approximately 30 μm. Subsequently, a 3D image of the entire specimen was generated by using all the above-mentioned 2D images. The post-processing software assigned a grey value to each voxel, from 0 (which belongs to the least dense voxel, i.e. void) to 255 (which belongs to the densest voxel, i.e. steel). The data from the scanning process was saved in a file that included the X, Y, and Z Cartesian coordinates of the voxel center of gravity and an integer number, from 0 to 255, with regards to its density. The total number of voxels in a specimen was approximately $2.4 \cdot 10^9$.

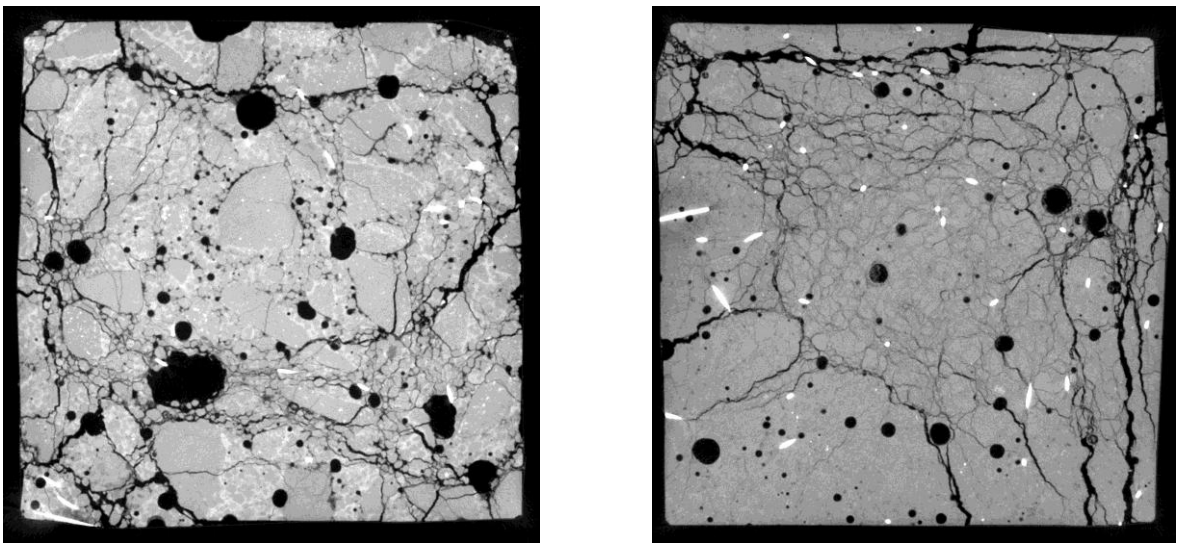

Figure 3: Slices belonging to different mixtures. From left to right: A-Series and B-Series.

The next step in this process was to identify and isolate each individual fiber within the specimen by image analysis software. First, the software identified the voxels of the fibers, which exhibited a range of grey values. In this case, after the grey scale histogram had been studied, the fibers were deemed to be within a range of between approximately 110 and 255 (Figure 4).

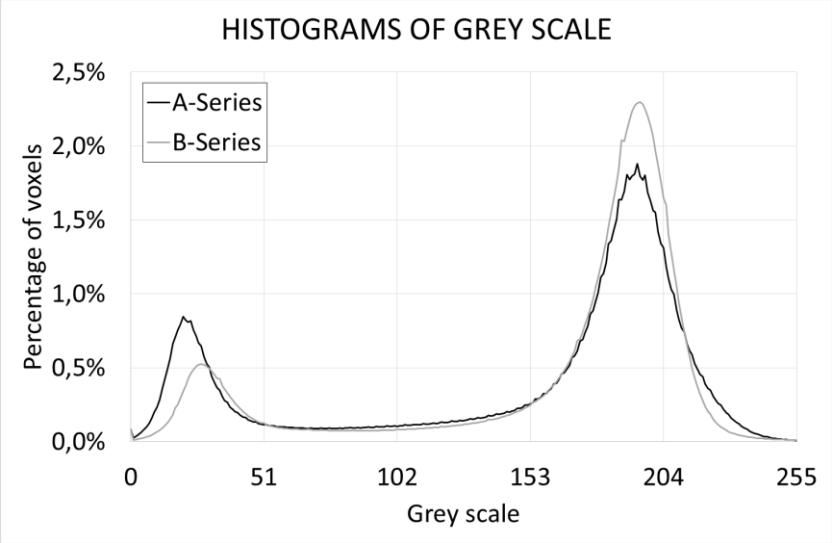

Figure 4: Histograms of grey scale.

Subsequently, all the voxels in contact were merged, since they originated from the same fibers. The software identified and isolated the different fibers (Figure 5).

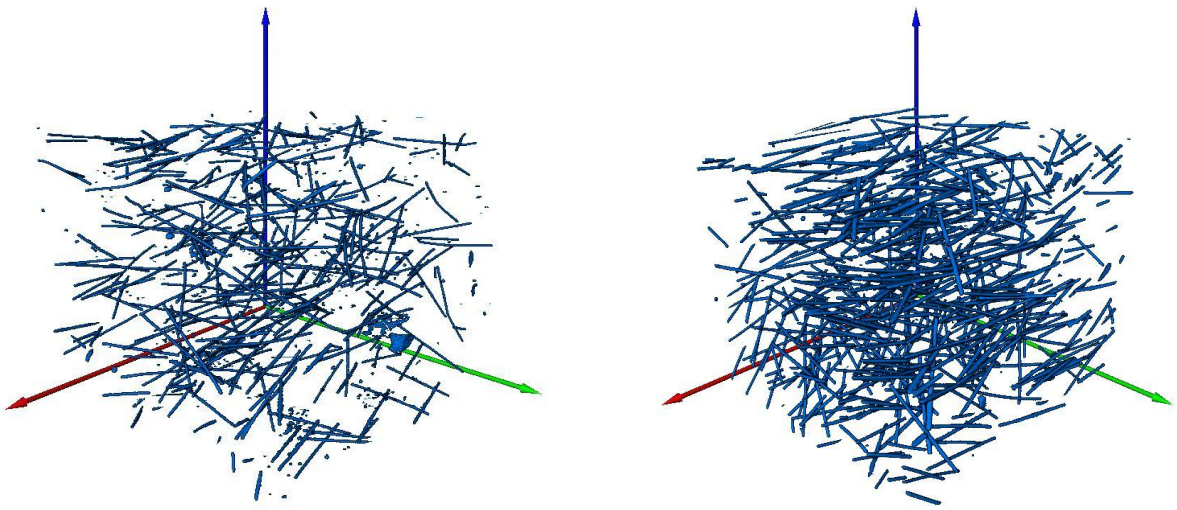

Figure 5: 3D views of the fibers belonging to different series. From left to right: A-Series and B-Series.

The result of this image analysis was a dot matrix containing the Cartesian coordinates X, Y, and Z at the center of gravity of each fiber, the fiber length, and orientation.

Once all the fibers had been identified and isolated, those showing a length of less than 2 mm were discarded due to the fact that they probably had originated in the denser inlays (even perhaps inside the aggregates) and to short portions of

fiber (usually as a result of the process of cutting close to the borders of the specimen). Nevertheless, these "short fibers" had no influence on the mechanical behavior of the concrete specimens.

The CT-Scan device provides an enormous amount of useful information. However, it is not possible to draw conclusions solely by direct observation of the 3D images. The data must be post-processed by using Digital Image Processing (DIP) software and/or post-processing sub-routines.

All the scans were performed once the specimen had undergone mechanical testing (i.e. static and cyclic compressive tests until failure).

3. EXPERIMENTAL RESULTS

In this section, the results of the CT-Scan and the static and fatigue tests are presented. Moreover, both the results from the CT-Scan and the mechanical tests are correlated.

3.1 CT-Scan analysis

The CT-Scan analysis was performed with AVIZO (FEI Visualization Sciences Group, Hillsboro, OR, USA) visualization and analysis software in combination with customized sub-routines.

3.1.1 Fiber orientation and content

Fiber orientation and content were the most important points of information gained from the CT-Scan analysis in this research. It was expected that not only would they exert a relevant influence on the macroscopic behavior of the specimens, but also on the natural scatter of the macroscopic behavior of the specimen, which could be partially explained by the intrinsic scatter of the fiber orientation and content. The AVIZO software generates two angular values θ (theta), and φ (phi) (Figure 6a). Theta is a polar angle, that is, the angle between the main axis (or the length) of the fiber and the Z axis. It should be noted that the vertical axis corresponds to the concrete direction and loading direction. Phi is an azimuthal angle, i.e., the angle between the projection of the main axis on the XY plane and X axis. Theta can vary between 0º and 90º while phi can vary between -90º and 90º.

Using this information, the orientation of the fiber according the Cartesian angles, α (alpha), β (beta) and γ (gamma) was obtained (Figure 6b).

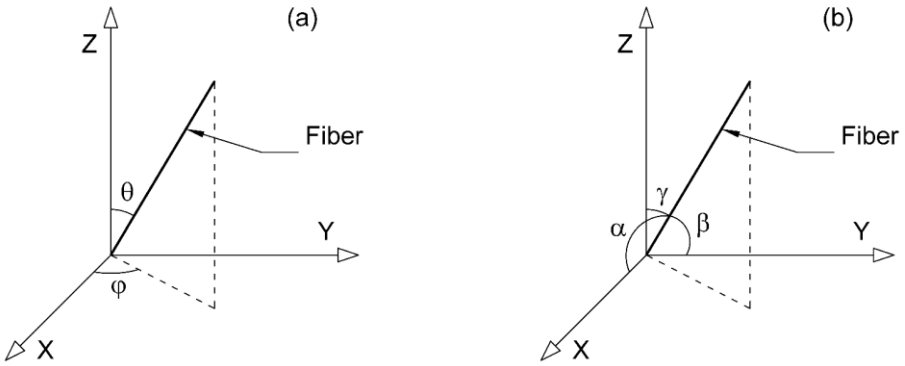

Figure 6: Identification of θ (theta) and φ (phi) angles in the Spherical coordinates (a) and of α (alpha), β (beta) and γ (gamma) in Cartesian coordinates (b).

The average histograms of angle distribution are shown in Cartesian coordinates, for both series (Figures 7 and 8). In these cases, the relative frequency is defined as the ratio between the number of fibers within the angular range and the average number of fibers of the specimen. As a consequence, the histograms include the effect of the amount of fiber on the fiber distribution. Fiber orientation does not vary during either static or fatigue tests. In this case, information shown in Figures 7and 8 have been extracted from the specimens prior to testing.

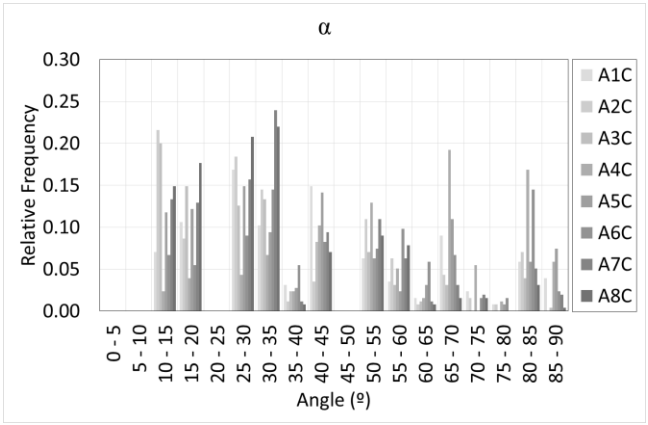

(a) Alpha angle in static tests

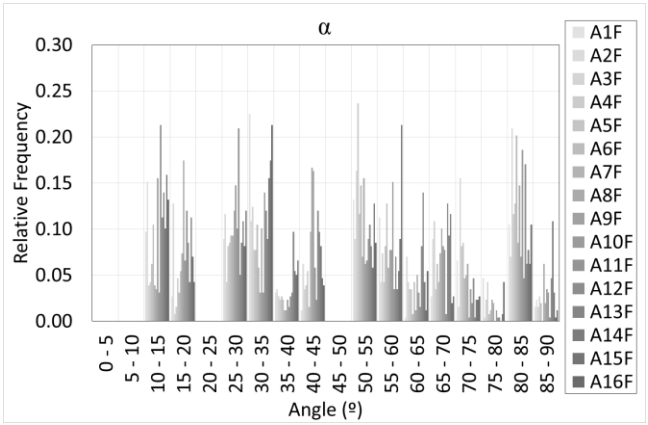

(b) Alpha angle in fatigue tests

Table 6: Statistical parameters of compressive strength and fatigue life for both series.

Statistical Parameters		A-Series		B-Series	
		Compression	Fatigue	Compression	Fatigue
f_c (MPa)	λ	0.018		0.008	
	k	7.970		21.922	
	R^2	0.743		0.917	
log(N)	λ		0.302		0.236
	k		3.154		7.437
	R^2		0.963		0.879

Table 7: Statistical parameters of fiber orientation and fiber content for both series.

Statistical Parameters		A-Series			B-Series		
		Compression	Fatigue	All	Compression	Fatigue	All
ei_α	μ	0.696	0.621	0.646	0.733	0.695	0.707
	σ	0.119	0.113	0.115	0.165	0.164	0.164
	CV	17%	18%	18%	22%	24%	23%
ei_β	μ	0.481	0.533	0.516	0.378	0.437	0.418
	σ	0.083	0.097	0.093	0.130	0.082	0.098
	CV	17%	18%	18%	34%	19%	23%
ei_γ	μ	0.292	0.332	0.319	0.341	0.331	0.334
	σ	0.058	0.046	0.050	0.084	0.057	0.066
	CV	20%	14%	16%	25%	17%	20%
fiber content (%)	μ	0.18%	0.19%	0.19%	0.50%	0.51%	0.51%
	σ	0.01%	0.02%	0.02%	0.04%	0.04%	0.04%
	CV	5%	11%	9%	8%	8%	8%

Table 6 and 7 present some interesting findings. First, the compressive strength shows very low scatter in both the A- and the B-Series. A similar phenomenon occurs in the case of fatigue life.

Furthermore, even though all the specimens of one series were extracted from the same prism, a relevant scatter in the fiber orientation was observed. Accordingly, all the efficiency indexes showed a significant scatter, with an average Coefficient of Variation (CV) of approximately 20% or greater. In this case, both series showed a similar scatter and a similar average value.

Additionally, the fiber content showed a significant scatter, with an average CV of approximately 9.1% in the case of A-series and 7.6% in the case of B-series. A slight difference could be observed between both series.

It is expected that the scatter observed in the fiber content and orientation is at least partial underlying reason for the scatter observed in the compressive strength and fatigue life.

3.3 Correlation between compressive strength and fiber orientation and content

Due to the mixture differences the A- and B-Series showed a different fiber content and, overall, a very different compressive strengths. The A-Series mixture can be described as a "conventional" high strength concrete, while the B-Series mixture can be defined as an ultrahigh strength concrete. Figure 10 set forth the correlations between the compressive strength f_c and the fiber orientation index.

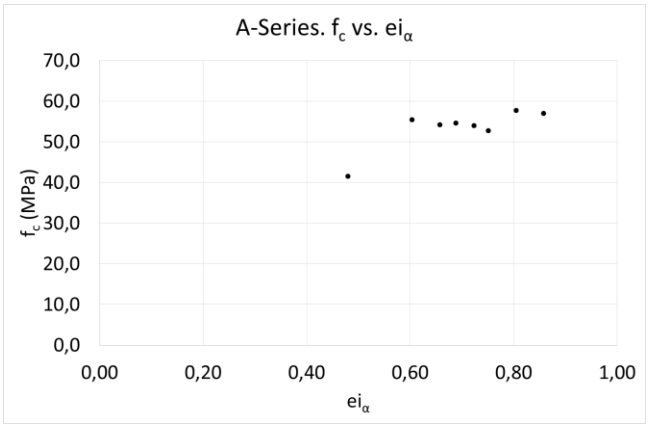

(a)

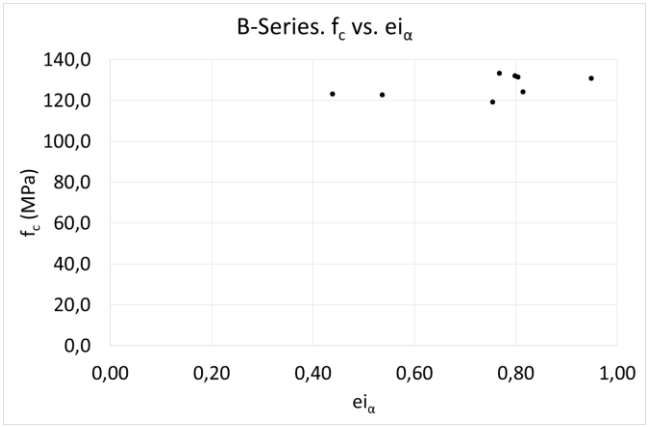

(b)

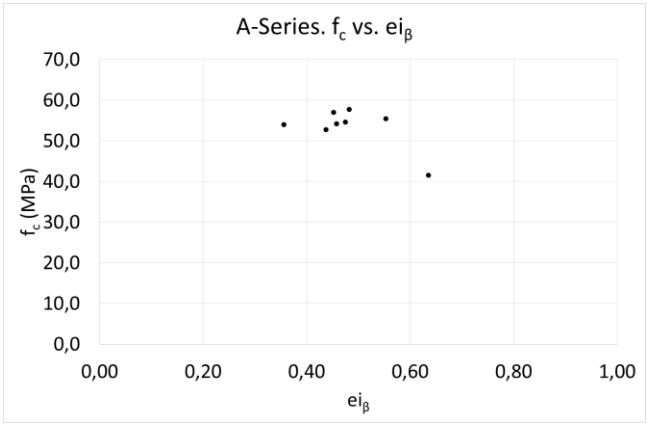

(c)

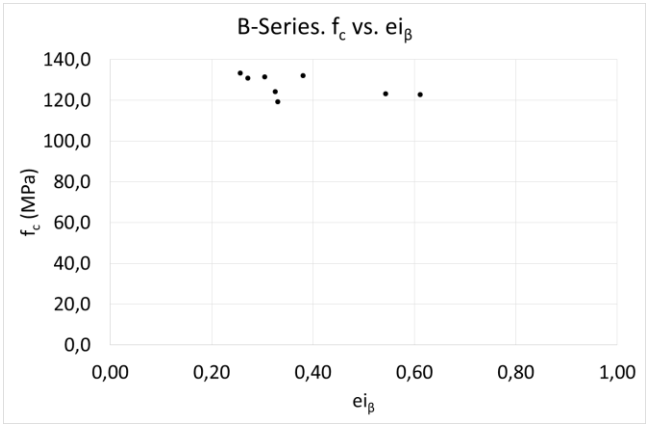

(d)

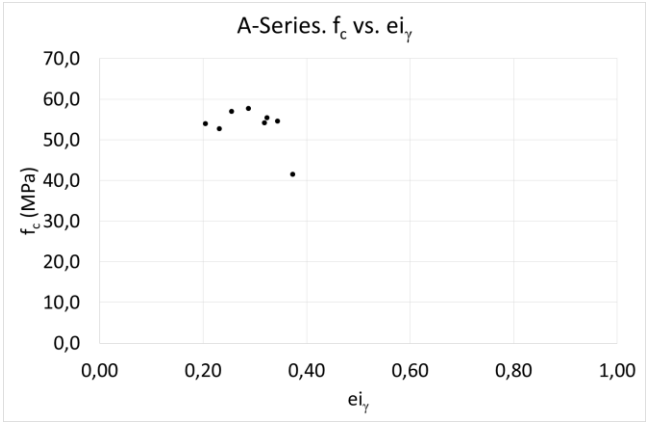

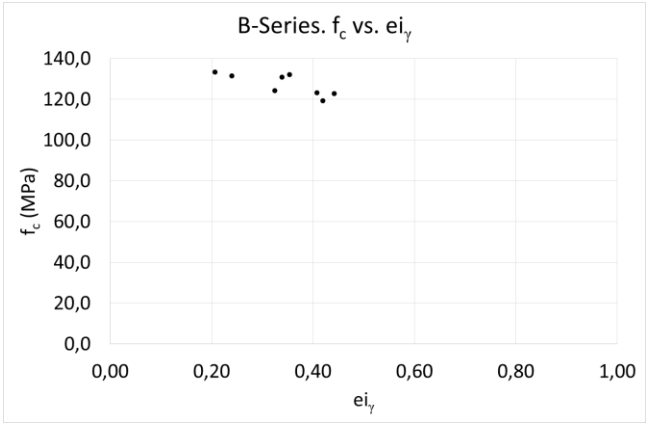

3.3 Correlation between compressive strength and fiber orientation and content

Due to the mixture differences the A- and B-Series showed a different fiber content and, overall, a very different compressive strengths. The A-Series mixture can be described as a "conventional" high strength concrete, while the B-Series mixture can be defined as an ultrahigh strength concrete. Figure 10 set forth the correlations between the compressive strength f_c and the fiber orientation index.

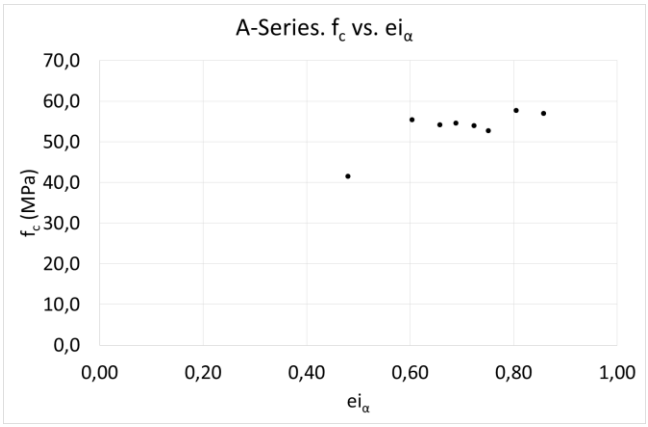

(a)

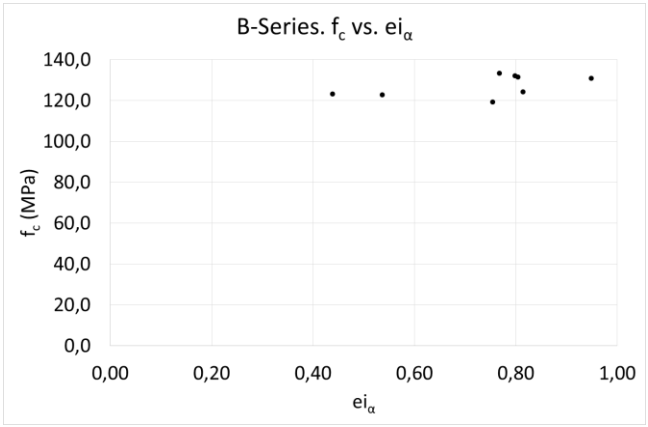

(b)

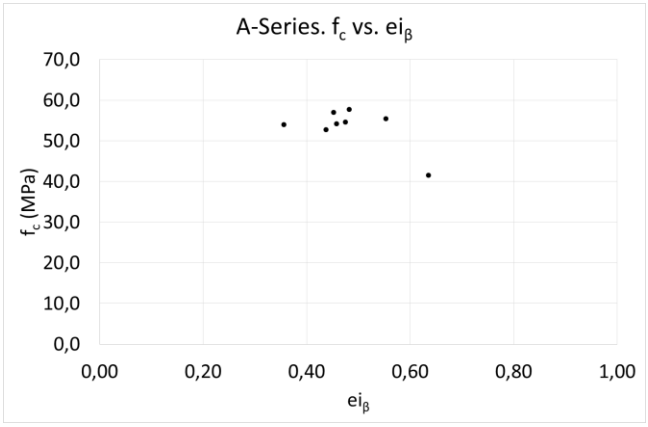

(c)

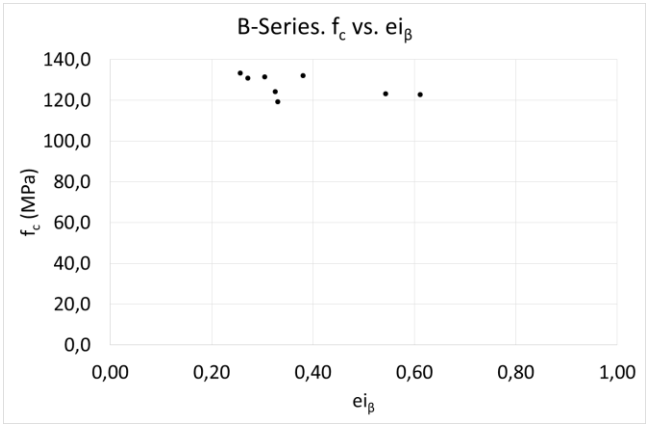

(d)

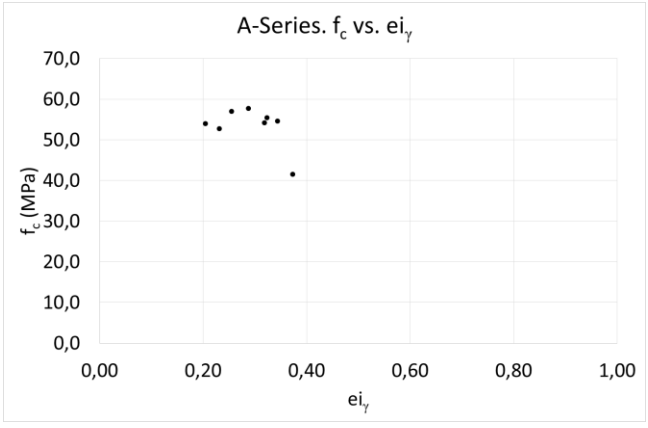

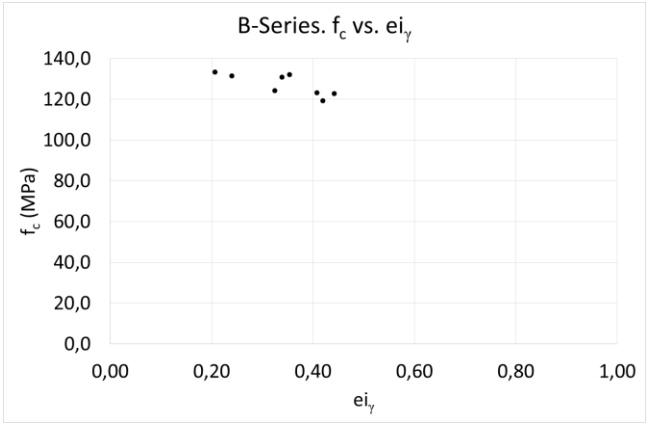

(e) (f)

Figure 10: Correlation between f_c and the efficiency indexes. From top to bottom, (a) and (b) $f_c\ vs. ei_\alpha$, (c) and (d) $f_c\ vs. ei_\beta$ and (e) and (f) $f_c\ vs. ei_\gamma$. From left to right, (a), (c) and (e) A-Series, (b), (d) and (f) B-Series.

Figure 10 reveals some interesting results. First, it can be observed that there is an inverse relationship between f_c and ei_γ in such a way that the smaller the efficiency index ei_γ, the greater the f_c. However, this is not a very strong relationship. It can be more clearly observed in the case of B-Series but in the case of A-Series this tendency is less clear. It should be remembered that a smaller value of ei_γ signifies that the fibers tend to be more perpendicular to the Z axis, i.e., more perpendicular to the concreting and loading direction. It is well known that compressive loads cause cracks parallel to the compression direction [28, 29]. In this case, when the fibers are placed more perpendicular to the cracks, thereby bridging them, this provides extra compressive strength to the specimen. In some way, the defined efficiency index is more an "inefficiency index". Therefore, the greater the index is, the lower the compressive strength. On the contrary, Figure 10 shows that there is no relationship between f_c and ei_α and ei_β.

3.4 Correlation between fatigue life and fiber orientation and content

As explained previously, the expected theoretical fatigue life "N" for the A-Series was 3,162 cycles, while the one for the B-Series was 398 cycles, according to Model Code 2010 [3]. Subsequently, the correlations between the fatigue life and fiber orientation and fiber content are presented (Figure 11).

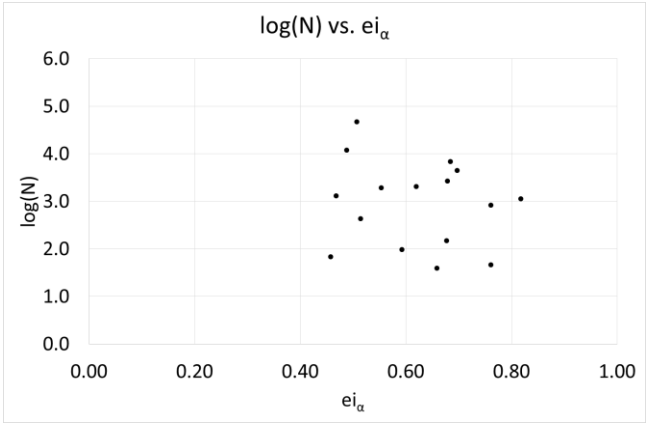

(a)

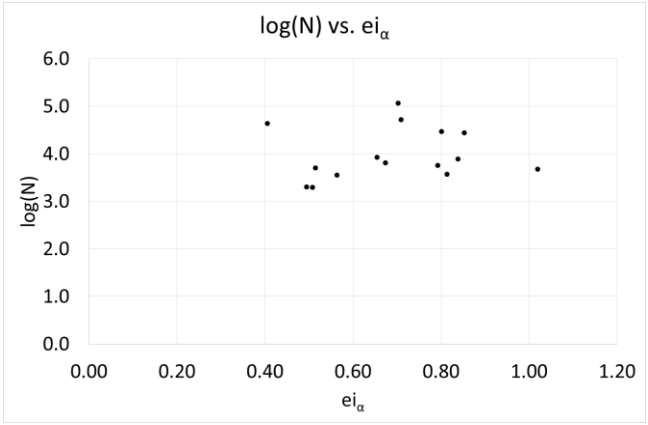

(b)

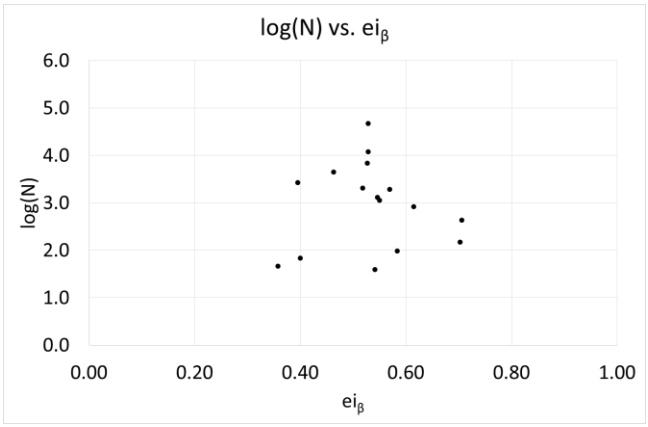

(c)

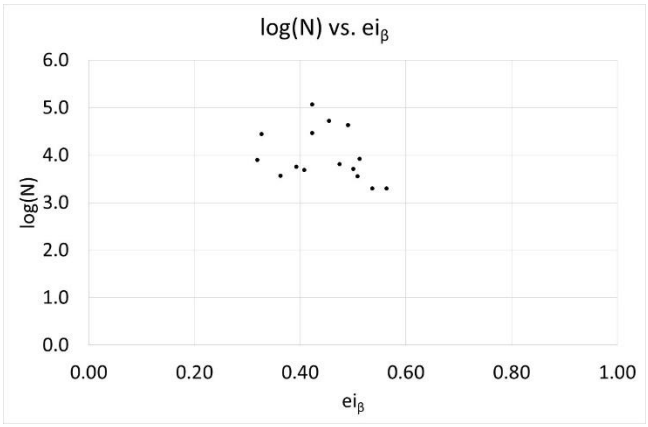

(d)

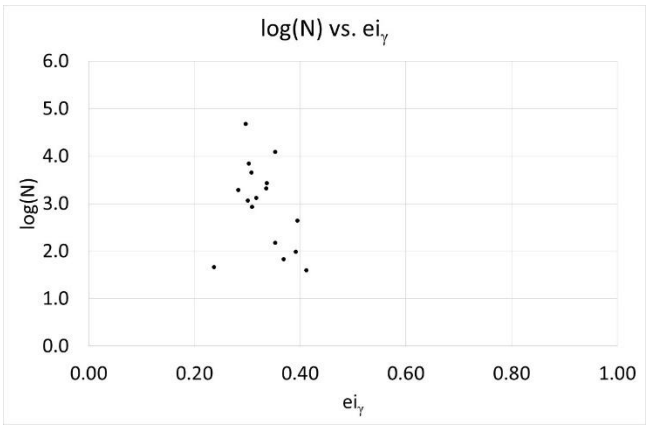

(e)

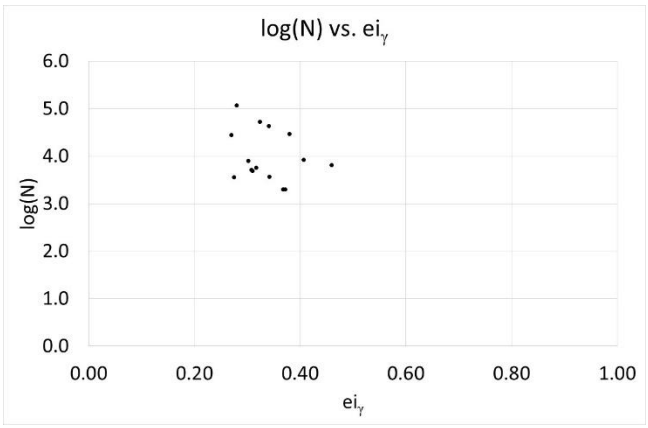

(f)

Figure 11: Correlation between fatigue life and the efficiency indexes. From top to bottom: (a) and (b) $\log(N)\ vs.\ ei_\alpha$, (c) and (d) $\log(N)\ vs.\ ei_\beta$ and (e) and (f) $\log(N)\ vs.\ ei_\gamma$. From left to right, (a), (c) and (e) A-Series, (b), (d) and (f) B-Series.

Figure 11 shows some very interesting results. Firstly, it can be noticed that Figure 11 (e) and (f) reveal that there is an inverse relationship as well between fatigue life and ei_γ in such a way that the smaller the efficiency index ei_γ, the greater the fatigue life. This tendency can be more clearly observed in the A-Series than in the B-Series. Moreover, when the fibers are placed more perpendicular to the cracks, the specimen will obtain longer fatigue life [16, 30-32] and higher compressive strength as shown in Figure 10 and 11. Furthermore, no relationship between fatigue life and ei_α and ei_β is found, which is similar to the compressive strength.

To better understand the correlation between fatigue life and ei_γ, the results have been plotted in a $\log(N)\ vs\ ei_\gamma$ plane (Figure 12). In these graphs, the contour curves correspond to equal values of the normal density function, that is, to points with the same probability of occurrence (also referred to as iso-probability curves).

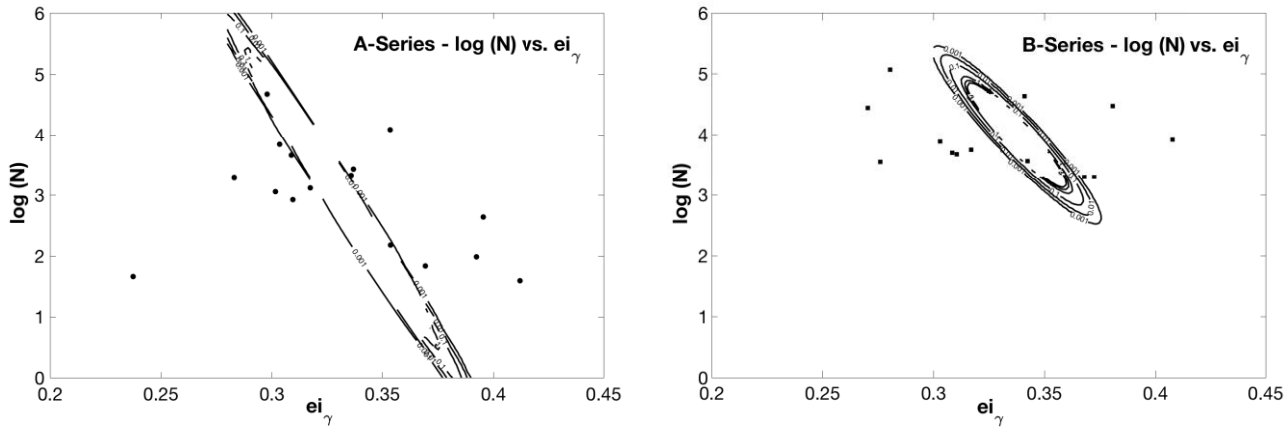

Figure 12: Correlation between fatigue life and ei_γ. Iso-probability curves

To examine more extensively, the correlation between the two variables, it is important to calculate the covariance matrices of the two series as well as their second invariant σ_{II} (eq. 2 and 3).

A-Series $$CovEc = \begin{pmatrix} 0.0021 & -0.0145 \\ -0.0145 & 0.8276 \end{pmatrix} \qquad \sigma_{II} = 0.0015 \qquad (2)$$

B-Series $$CovEc = \begin{pmatrix} 0.0028 & -0.0072 \\ -0.0072 & 0.2964 \end{pmatrix} \qquad \sigma_{II} = 0.0008 \qquad (3)$$

With this information, it is clear that the correlation between both variables is inverse for the two series, A and B, since the values outside of the main diagonal of the matrices are negative. Furthermore, these outer diagonal values show that the correlation is stronger in the A Series than in the B-Series, which is an assertion confirmed by a higher value of the second invariant, σ_{II}, for the A-Series.

Figure 12 shows that the iso-probability curves are similar to ellipsoids with a main axis following a decreasing tendency with ei_γ, which supports the observations previously described, i.e., the more perpendicular the fibers are with respect to the cyclic load, the greater the fatigue life.

4. RESISTANCE MECHANISMS

The results described above reveal that the fiber content and orientation have a positive impact on the behavior of concrete under both static and cyclic compressive loads. The conventional explanation is that the fibers sew the cracks, thereby providing extra structural capacity, resulting in a slightly higher compressive strength under static compressive loads and a higher fatigue life under compressive cyclic loading.

Using the CT-Scan technology, both the resistance and the failure mechanisms inside the specimens may be observed, in order to gain a better functional understanding of fibers.

As explained previously, the A-Series was a conventional high strength concrete, with an average compressive strength of around 54 MPa. In this series, very noticeable damage was observed inside the specimen, in both static and cyclic tests (Figure 13). Many cracks were observed, following an apparently random distribution along a horizontal plane. They tended to follow a vertical plane, which is parallel to the compressive load. However, greater content of cracks was found close to the specimen surfaces. Most of the cracks had a small width and a short length. There were no differences between the crack patterns of the specimen subjected to static and cyclic loads, as demonstrated by Vicente et al. [16].

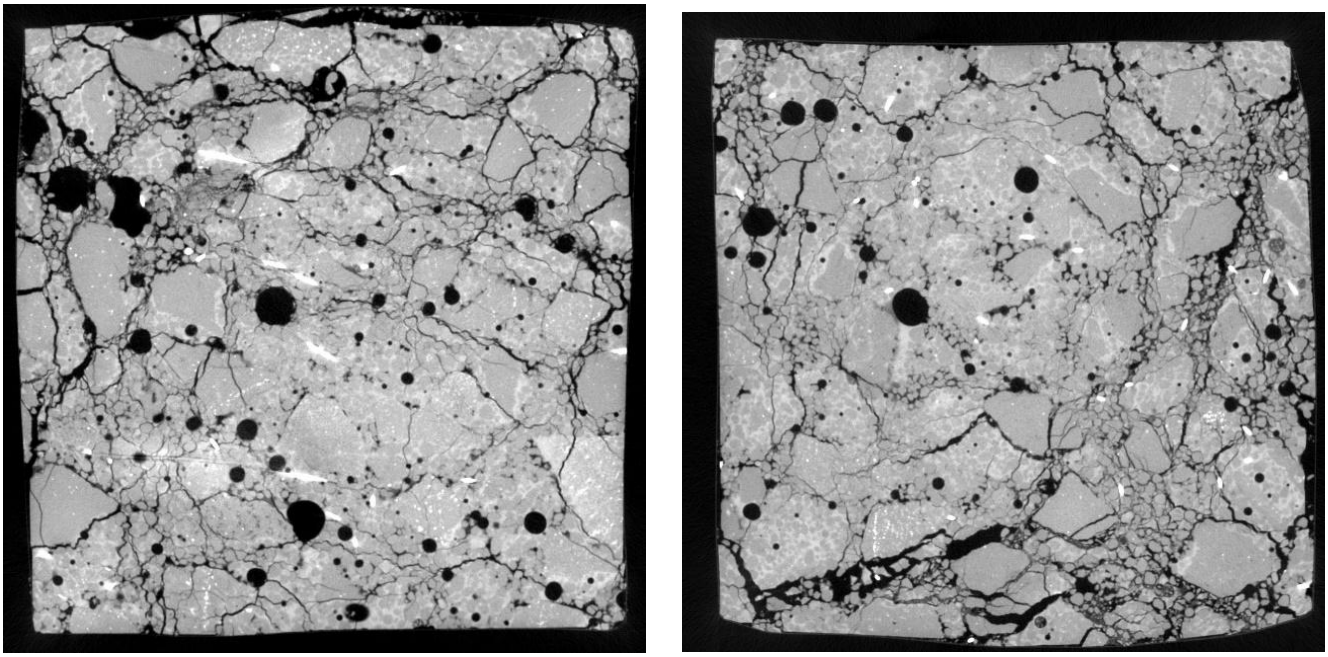

(a) Static tests (b) cyclic tests

Figure 13: Typical crack patterns in A-Series.

The B-Series was made with ultra-high strength concrete, with an average compressive strength of approximately 128 MPa, that is, more than twice the compressive strength of the A-Series and with a higher fiber content. In this case, it can be observed that the damage was less severe inside the specimen, in both the static and the cyclic tests (Figure 14). In this case, there are in general, few cracks, and in particular, very few small cracks, which denotes a higher fragility of the concrete mixture. Moreover, the cracks tended to be straight on the horizontal plane (and they also tended to follow a vertical plane, which was parallel to the compressive load), unlike what occurred with the A-Series where the cracks tended to meander. The result is that B-Series shows a smaller crack surface and consequently less ductility. Furthermore, the maximum size of aggregate is 8 mm for the A-Series, while it is 2 mm for the B-Series, thus, the granular structures of them are quite different. This would be another relevant reason resulting in the differences in the crack propagation.

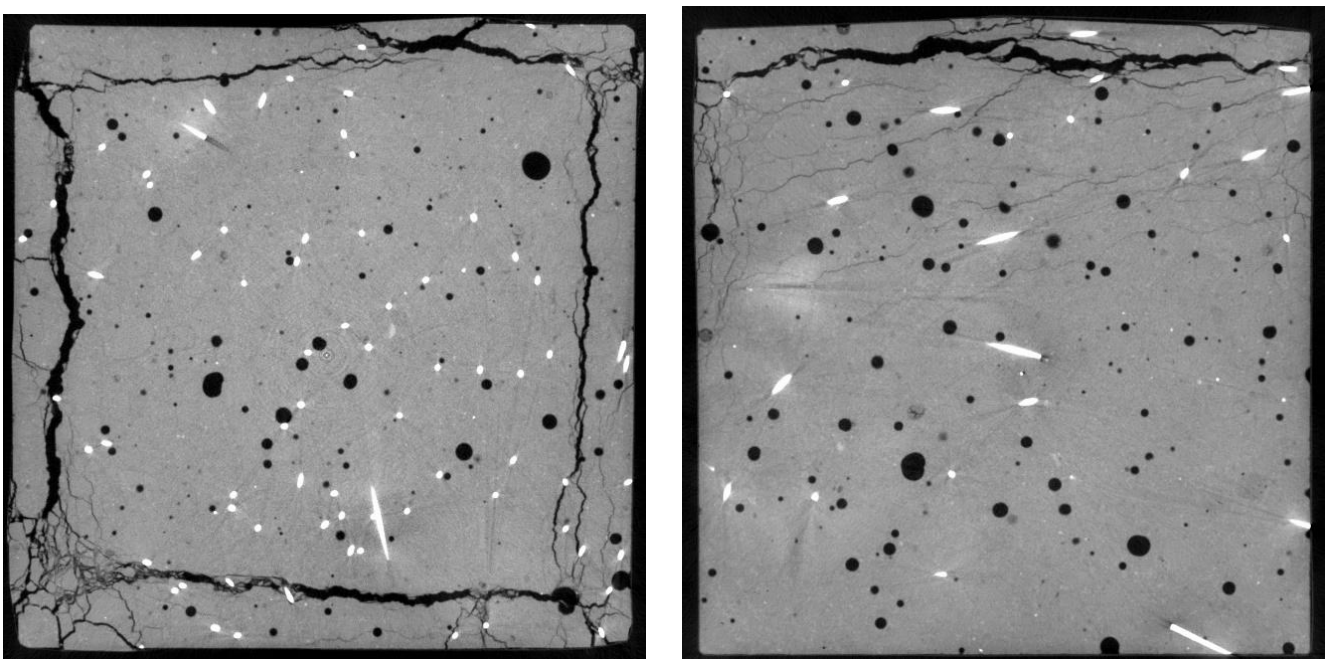

(a) Static tests (b) cyclic tests

Figure 14: Typical crack patterns in B-Series.

In all cases, the fibers showed good bonding properties. This implies that when the crack crossed through the central region of the fiber (i.e., not very close to the ends), it appropriately sewed the crack, thereby helping it to withstand the compressive load. In some cases, the cracks surrounded some fibers that were no longer able to work (Figures 15 and 16).

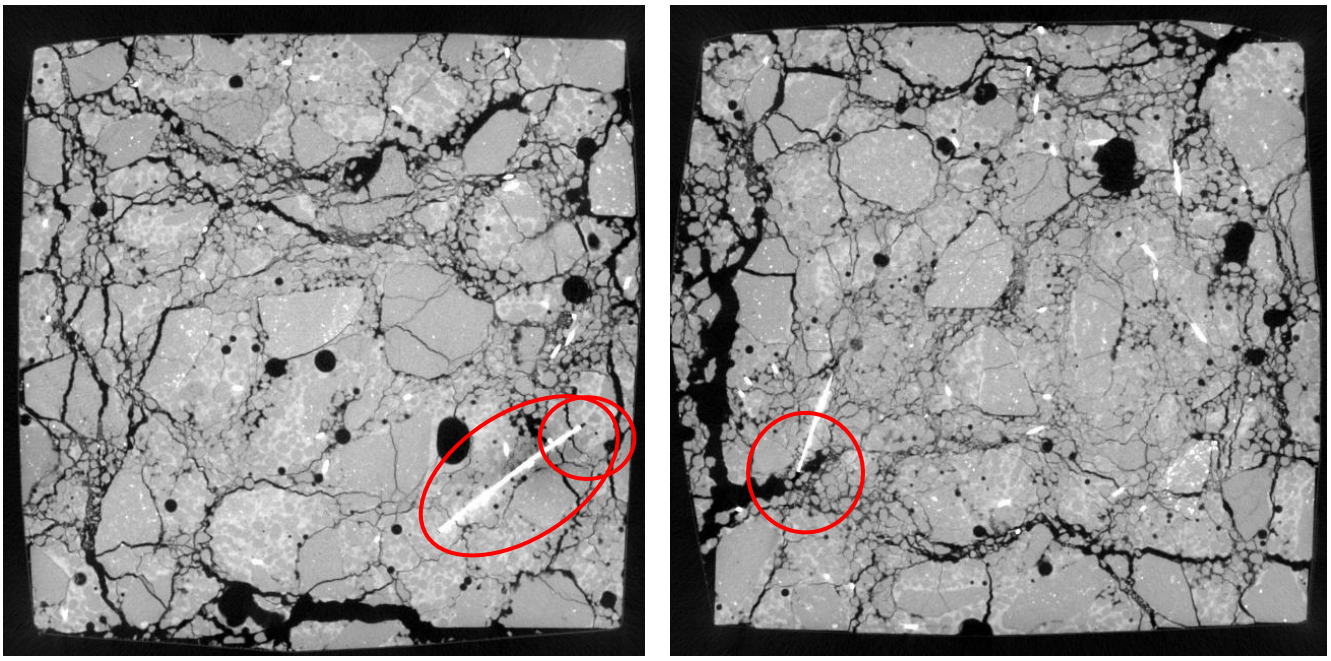

(a) (b)

Figure 15: Different types of behavior of the fibers in the A-Series. On the left (a), good behavior (the crack crosses the fiber through its central region). On the right (b), bad behavior (the crack surrounds the fiber)

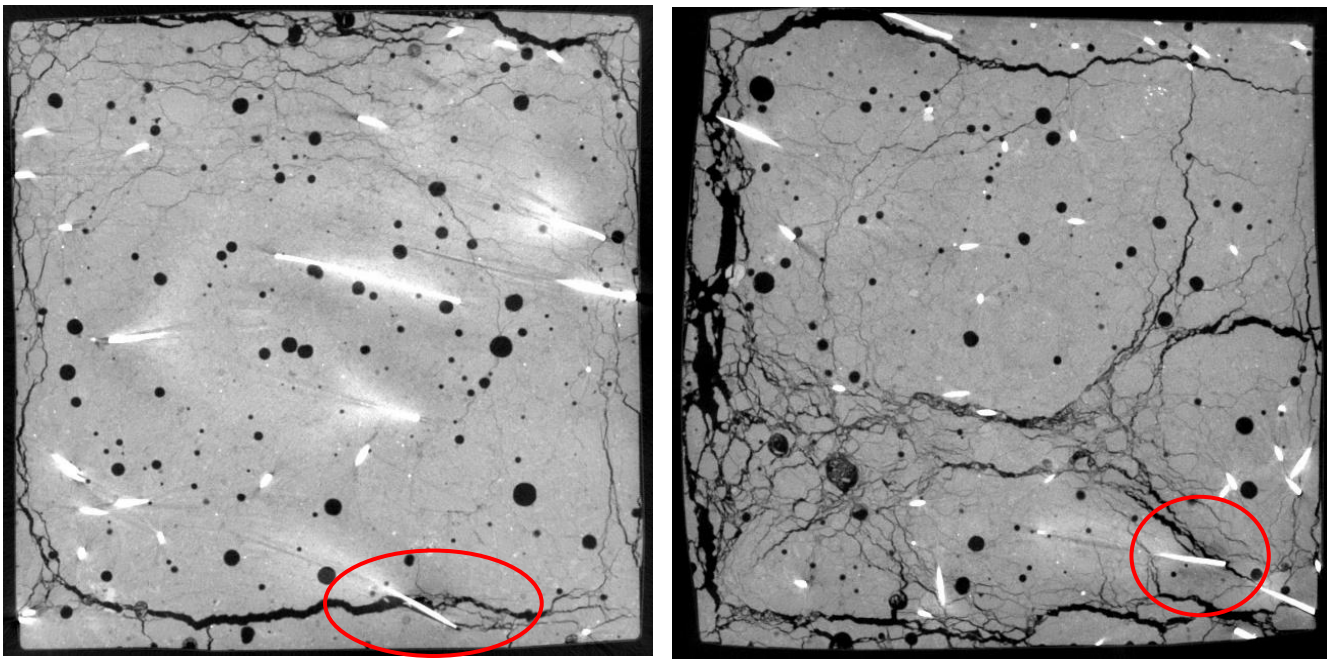

(a) (b)

Figure 16: Different types of behavior of the fibers in the B-Series. On the left (a), good behavior (the crack crosses the fiber through its central region). On the right (b), bad behavior (the crack surrounds the fiber)

As can be observed in Figures 15a and 16a, the marked fiber shows proper behavior, thereby fixing the crack. A small displacement can be observed at the end of the fiber, thereby causing a small hole behind it. In the case of the A-Series, the size of this hole was almost identical to the crack width, thereby indicating that the fiber showed no elongation. On the contrary, in the case of the B-Series the size of the hole behind the fiber appeared to be a bit smaller than the crack width, which indicated an elongation of the fiber. These results are logical in so far that the specimens of the B-Series were subjected to higher stress levels due to their higher compressive capacity.

On the contrary, Figures 15b and 16b show examples of where the cracks surround the fibers, actually weakening their bond.

In general, the CT-Scan images showed that the resistance mechanisms of the fibers were identical to conventional rebars, although on a different scale. Accordingly, the fibers needed an anchorage length to be able to work efficiently. Where the crack crossed the fiber very close to its ends, that is, within the anchorage length, a debonding failure could be observed. In some cases, the crack surrounded the fiber, as previously explained (Figures 17a and 18a), resulting in a

complete loss of adherence. In other cases, there was an intense microcracking in the area surrounding the anchorage of the fiber, resulting in a partial loss of adherence and in an increase in the effective anchorage length (Figures 17b and 18b).

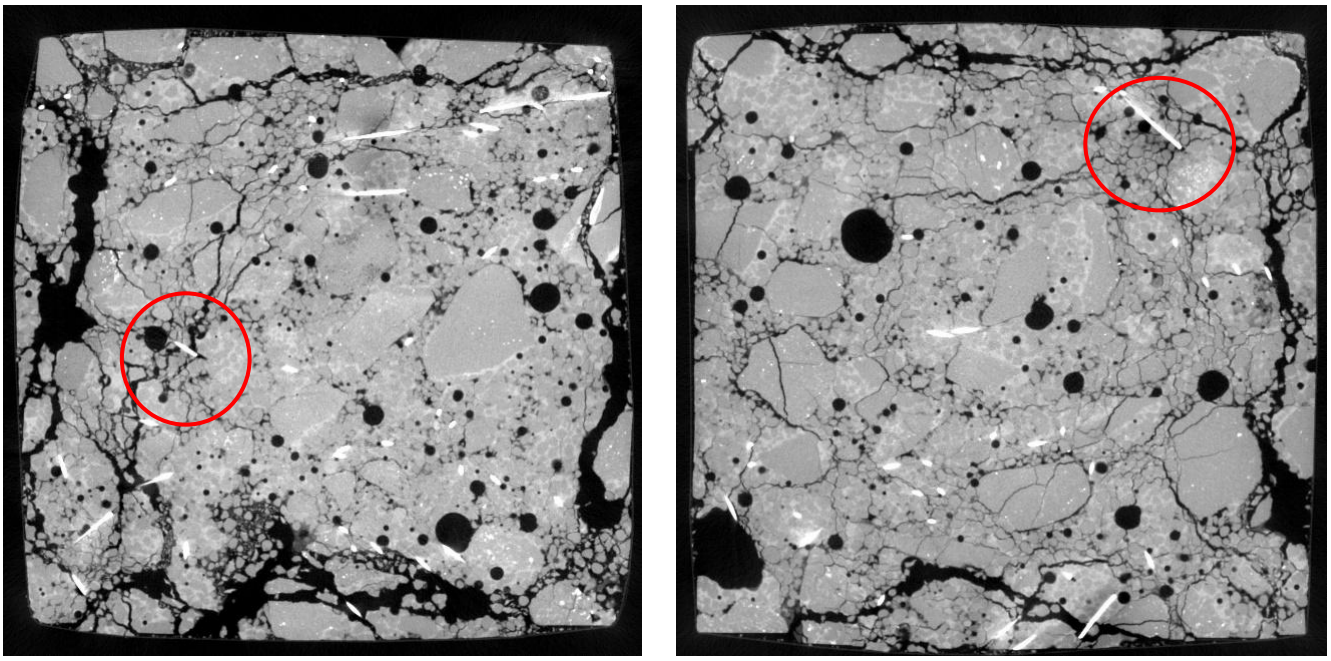

(a) (b)

Figure 17: Different types of behavior of the fibers in the A-Series. On the left (a), a complete loss of adherence, (the crack surrounds the fiber). On the right (b), a partial loss of adherence, (an intense microcracking in the area at the end of the fiber is observed)

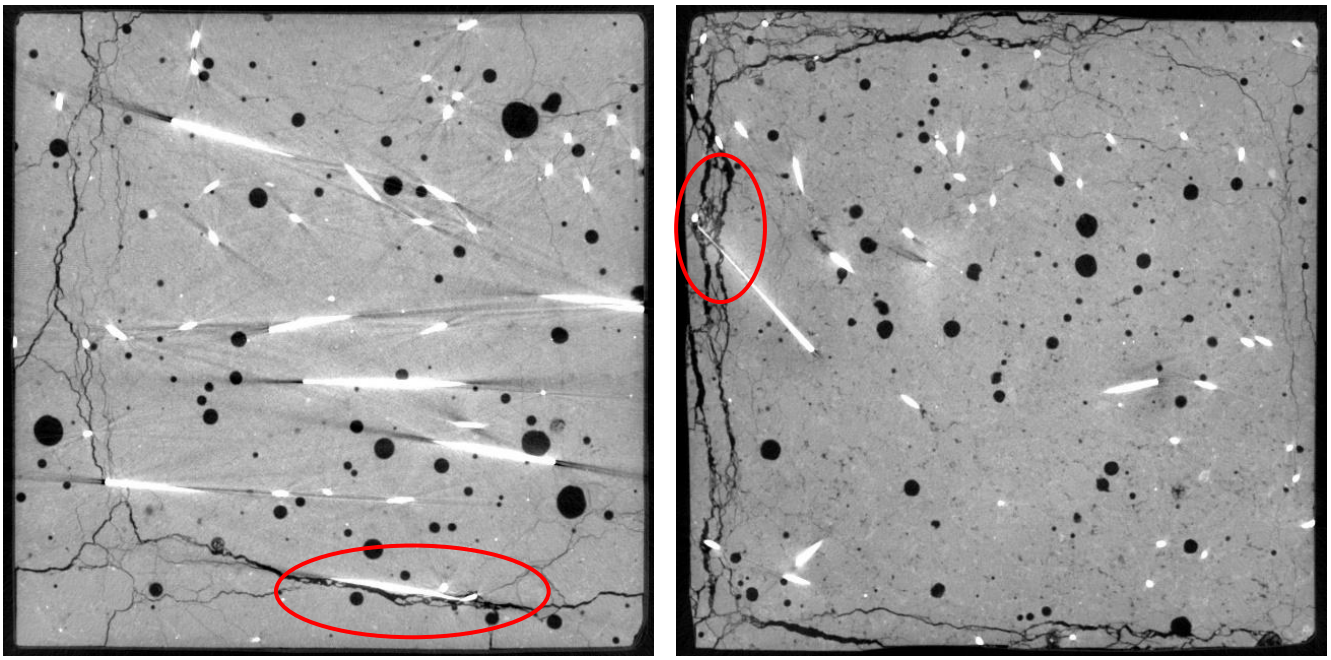

(a) (b)

Figure 18: Different types of behavior of the fibers in the B-Series. On the left (a), a complete loss of adherence, (the crack surrounds the fiber). On the right (b), a partial loss of adherence, (an intense microcracking in the area at the end of the fiber is observed)

In many cases, small pores at the end of the fiber were observed (Figure 19). These pores acted as catalysts of the cracks, arising at these points. Unfortunately, these cracks were the ones which surround the fibers, resulting in a loss of efficiency of the fiber.

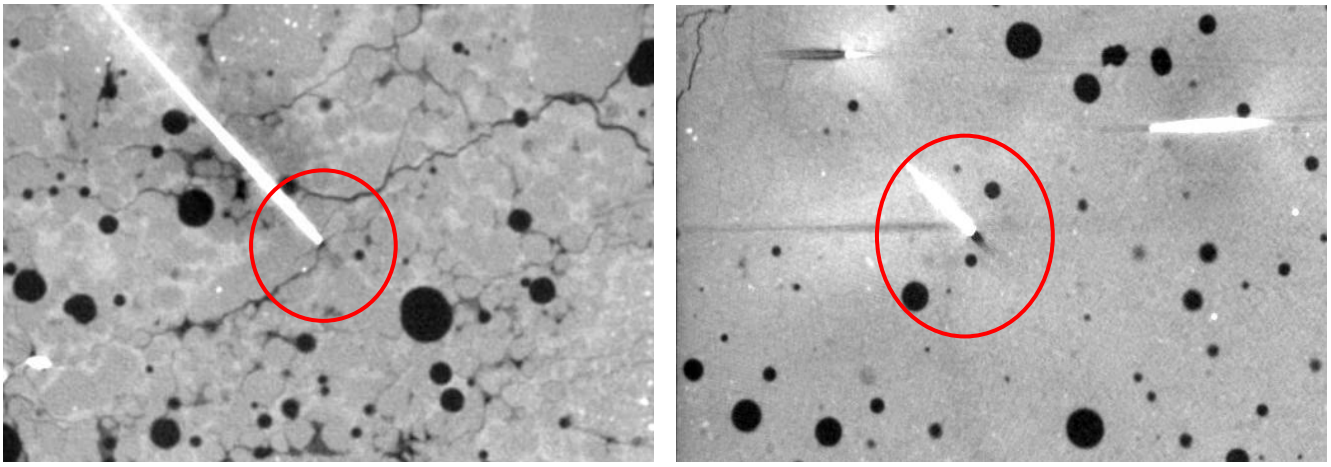

(a) (b)

Figure 19: Detailed view of a pore at the end of the fiber and the emergence and initial growth of a small crack. On the left (a), A-Series. On the right (b), B-Series

Both series showed the same failure mechanisms and no significant differences were observed. These results coincided with those observed by Vicente et al. [33] in the case of steel fiber-reinforced concrete prisms subjected to three-point bending tests. The main difference was that in this case, no fiber breakage was observed, while the collapse was widely observed in the research performed by Vicente and co-workers [33]. The explanation in this case is that where external compressive loads were applied, internal tensile forces were not very relevant while in the case of external tensile (or flexural) loads, internal tensile forces were higher and could lead to fiber breakage.

5. CONCLUSIONS

This study has inquired into the well-known intrinsic scatter compressive strength of concrete specimens and their fatigue life. In particular, it has focused on steel fiber-reinforced high and ultra-high strength concrete. In all specimens, both the fiber orientation and fiber distribution exhibited intrinsic scatter, which offers partial explanations for the scatter in the macroscopic behavior of concrete and therefore, the scatter in both its compressive strength and fatigue life.

First, the results have shown that the intrinsic scatter of fiber orientation and content has a small impact on the compressive strength of concrete, which shows that compressive strength mainly depends on the base concrete. That is to say, steel fibers have a negligible effect on compressive strength, which coincides with other experimental studies where the fiber content is less than 2% [34-36]. However, fiber orientation and content have a greater impact on fatigue life, indicating that fatigue life not only depends on base concrete, but also on fiber orientation and content.

In all cases, the most relevant orientation was the one with respect to the Z axis, which is to say with respect to the loading axis. In this case, the more perpendicular the fibers are to the Z axis, the better their behavior. The influence of fiber orientation on the horizontal plane (along the X and Y axes) is not appreciable.

The CT-Scan images have shown how fibers collaborate to improve the concrete capacity. In general, the fibers bridged the cracks properly, although the cracks often surrounded the fibers, inhibiting their mechanical capacity.

It was also observed that the ends of the fibers were common places to the presence of small pores. These pores acted as "catalysts" for the origin and growth of the cracks, reducing the efficiency of the fibers.

The resistance mechanisms of the fibers and the failure modes observed in these specimens, subjected to static and cyclic compressive loads were similar to those observed in the concrete specimens subjected to three-point bending tests, except for the breakage of the fibers. This difference, in the case of the compressive tests, was due to the internal tensile forces that were not sufficiently high to break the fibers.

6. ACKNOWLEDGEMENTS

The authors are grateful for financial support from the Ministerio de Economía y Competitividad, BIA2015-68678-C2-R, Spain.

REFERENCES

[1]. American Concrete Institute. (2016). "Report on Design of Concrete Wind Turbines" ACI ITG-9R-16, Farmington Hills, MI, USA.

[2]. Det Norske Veritas. (2010). "Offshore concrete structures." DNV-OS-C502, Oslo, Norway.

[3]. International Federation for Structural Concrete. (2010). "Model code for concrete structures." FIB Bulletin 65, Lausanne, Switzerland.

[4]. American Concrete Institute (ACI). (1997). "Considerations for design of concrete structures subjected to fatigue loading (revised 1992/reapproved 1997)." ACI 215 R-74, Farmington Hills, MI, USA.

[5]. Moromi, I.; García, F.; Torre, A.; Espinoza, P.; Acuña, L. (2018). "Application of the Monte Carlo method to estimate the uncertainty in the compressive strength test of high-strength concrete modelled with a multilayer perceptron". Revista de la Construcción, v 17(2), pp. 319-329. https://dx.doi.org/10.7764/rdlc.17.2.319.

[6]. Meng, Q.; Wu, Y.; Xiao, J. (2018). "The effect of micro-structural uncertainties of recycled aggregate concrete on its global stochastic properties via finite pixel-element Monte Carlo simulation". Front. Struct. Civ. Eng., v 12(4), pp. 474–489.

[7]. Fairbairn, E.; Guedes, Q.; Ulm, F. (1999). "An inverse problem analysis for the determination of probabilistic parameters of concrete behavior modeled by a statistical approach". Materials and Structures, v. 32(215), pp. 9-13.

[8]. Liang, J.; Ding, Z.; Li, J. (2017). "A probabilistic analyzed method for concrete fatigue life". Probabilistic Engineering Mechanics, v. 49, pp. 13-21.

[9]. Ortega, J.J.; Ruiz, G.; Yu, R.; Afanador-Garcia, N.; Tarifa, M.; Poveda, E.; Zhang, X.; Evangelista, F. (2018). "Number of tests and corresponding error in concrete fatigue". International Journal of Fatigue, v 116, pp. 210-219.

[10]. Li, J. (2004). "Research on the stochastic damage mechanics for concrete material and structures (in Chinese)". J. Tongji Med. Univ. (National Science Edition), v 32 (10), pp. 1270-1277.

[11]. Breitenbücher, R.; Ibuk, H. (2006). "Experimentally based investigations on the degradation process of concrete under cyclic load". Materials and Structures, v 39(7), pp. 717-724.

[12]. Yang, D. (1994). "A distribution function for the fatigue life of concrete". Magazine of Concrete Research, v. 46(168), pp. 215-221.

[13]. Chen, H.; Xu, B.; Mo, Y.L.; Zhou, T. (2018). "Behavior of meso-scale heterogeneous concrete under uniaxial tensile and compressive loadings". Construction and Building Materials, v 178, pp. 418-431.

[14]. Tabsh, S.W.; Aswad, A. (1997). "Statistics of high-strength concrete cylinders". ACI Materials Journal, v 94(5), pp. 361-364.

[15]. Tarifa, M.; Ruiz, G.; Poveda, E.; Zhang, X.; Vicente, M.A.; González, D.C. (2018). "Effect of uncertainty on load position in the fatigue life of steel-fiber reinforced concrete under compression". Materials and Structures, v 15(31), doi:https://doi.org/10.1617/s11527-018-1155-6.

[16]. Vicente, M.A.; Ruiz, G.; González, D.C.; Mínguez, J.; Tarifa, M.; Zhang, X. (2018). "CT-Scan study of crack patterns of fiber-reinforced concrete loaded monotonically and under low-cycle fatigue". International Journal of Fatigue, v. 114, pp. 138-147.

[17]. Mínguez, J.; González D.C.; Vicente M.A. (2017). "Influence of fibre volume fraction and fibre orientation on the residual flexural tensile strength of fibre-reinforced concrete (In Spanish)". Hormigón y Acero, doi:http://dx.doi.org/10.1016/j.hya.2017.05.007.

[18]. Balazs, G.L.; Czoboly, O.; Lubloy, E.; Kapitany, K.; Barsi, A. (2017). "Observation of steel fibers in concrete with computed tomography". Construction and Building Materials, v. 140, pp. 534-541.

[19]. Pastorelli, E.; Herrmann, H. (2016). "Time-efficient automated analysis for fibre orientations in steel fibre reinforced concrete". Proceedings of the Estonian Academy of Sciences, v 65 (1), pp. 28-36.

[20]. Herrmann, H.; Pastorelli, E.; Kallonen, A.; Suuronen, J.P. (2016). "Methods for fibre orientation analysis of X-ray tomography images of steel fibre reinforced concrete (SFRC)". Journal of Materials Science, v 51(8), pp. 3772-3783.

[21]. Ponikiewski, T.; Katzer, J. (2016). "X-ray computed tomography of fibre reinforced self-compacting concrete as a tool of assessing its flexural behaviour". Materials and Structures, v. 49, pp. 2131-2140.

[22]. Ponikiewski, T.; Katzer, J.; Bugdol, M.; Rudzki, M. (2014). "Determination of 3D porosity in steel fibre reinforced SCC beams using X-ray computed tomography". Construction and Building Materials, v 68, pp. 333-340.

[23]. Vicente, M.A.; González, D.C.; Mínguez, J. (2014). "Determination of dominant fibre orientations in fibre-reinforced high strength concrete elements based on computed tomography scans". Nondestructive Testing and Evaluation, v 29(2), pp. 164–182.

[24]. Vicente, M.A.; Mínguez, J.; González, D.C. (2017). "The use of computed tomography to explore the microstructure of materials in civil engineering: from rocks to concrete". In: Halefoglu Ahmet Mesrur, editor. Computed tomography - advanced applications. InTech.

[25]. Vicente, M.A.; González, D.C.; Mínguez, J. (2019). "Recent advances in the use of computed tomography in concrete technology and other engineering fields". Micron, v 118, pp. 22-34.

[26]. European Committee for Standardization (2011). "EN 197-1. Cement – Part 1. Composition, specifications and conformity criteria for common cements". Brussels, Belgium.

[27]. European Committee for Standardization (2004). "EUROCODE 2, Design of concrete structures". Eurocode2, Brussels, Belgium.

[28]. Choi, S.; Shah, S.P. (1997). "Measurement of deformations on concrete subjected to compression using image correlation". Experimental Mechanics, v 37(3), pp. 307-313.

[29]. Lawler, J.S.; Keane, D.T.; Shah, S.P. (2001). "Measuring three-dimensional damage in concrete under compression". ACI Materials Journal, v 98(6), pp. 465-475.

[30]. Li, V.C. (1993). "Micromechanics of crack bridging in fibre-reinforced concrete". Materials and Structures, v 26, pp. 486-494.

[31]. Li, V.C.; Maalej, M. (1996). "Toughening in cement based composites. Part II. Fiber reinforced cementitious composites". Cement & Concrete Composites, v 18, pp. 239-249.

[32]. Lawler, J.S.; Wilhelm, T.; Zampini, D.; Shah, S.P. (2003). "Fracture processes of hybrid fiber-reinforced mortar". Materials and Structures, v 36, pp. 197-208.

[33]. Vicente, M.A.; Mínguez, J.; González, D.C. (2019). "Computed tomography scanning of the internal microstructure, crack mechanisms, and structural behavior of fiber-reinforced concrete under static and cyclic bending tests". International Journal of Fatigue, v 121, pp. 9-19.

[34]. Bentur, A.; Mindess, S. (2007). Fibre reinforced cementitious composites. London and New York: Taylor and Francis.

[35]. Ruiz, G.; De La Rosa, Á.; Wolf, S.; Poveda, E. (2018). Model for the compressive stress–strain relationship of steel fiber-reinforced concrete for non-linear structural analysis. *Hormigón y Acero*; v 69 (S1), pp. 75-80.

[36]. De La Rosa, Á.; Ruiz, G.; Poveda, E. Study on the compressive behavior of steel fiber-reinforced concrete based on the Surface Response Methodology. *Applied Sciences. Submitted*.